Journal of Zhejiang University-SCIENCE A
www.jzus.zju.edu.cn; www.springer.com/journal/11582
E-mail: jzus_a@zju.edu.cn

Research Article
https://doi.org/10.1631/jzus.A2600049

Numerical modeling for generating ultrahigh porosity aluminum foam through independent control of pore size and cell wall thickness

Peng GUO, Hanyu CHEN, Lifeng FAN✉

College of Architecture and Civil Engineering, Beijing University of Technology, Beijing 100124, China

Abstract: This paper proposed a numerical modeling method for generating ultrahigh porosity aluminum foam through independent control of pore size and cell wall thickness. The proposed method introduced two independently adjustable parameters (point spacing and scaling distance) to control pore size and cell wall thickness, respectively. Aluminum foam models with a porosity exceeding 90% were constructed while maintaining structural integrity using the proposed method, and the influence of key modeling parameters on the porosity of the models was discussed. The reliability of the modified method was validated by comparing both geometric morphology and dynamic mechanical properties between experimental aluminum foam samples and corresponding numerical models. The results indicate that the proposed method can effectively generate aluminum foam models with tailored pore sizes and wall thicknesses by adjusting the point spacing and scaling distance. The relative error in porosity between the experimental and numerical models is less than 3%, and the deviation in pore size distribution is within 10%. Furthermore, the numerical model demonstrates high accuracy in predicting dynamic mechanical behavior, with a relative error in yield stress as low as 1.2%. The consistent trends in the effects of pore size and cell wall thickness on dynamic mechanical properties further confirm the validity of the modeling approach.

Key words: High porosity; Voronoi structure; Numerical simulation; Dynamic mechanical properties; Pore structure control

1 Introduction

Aluminum foam is a lightweight porous metallic material characterized by a set of functional properties, including energy absorption, shock damping, thermal insulation, and heat dissipation (An et al., 2021; Xu et al., 2023), which have led to broad application in fields such as protective engineering and automotive transportation (Kumar et al., 2020; Hangai et al., 2022). The macroscopic performance of aluminum foam is largely attributed to its complex internal porous architecture, where energy dissipation occurs primarily through the substantial deformation of individual pores (Huang et al., 2023). Understanding the relationship between this intricate microstructure and the resulting macroscale properties often relies on the development of numerical models capable of accurately representing its internal geometry (Rajendran et al., 2009; He et al., 2024). Consequently, establishing a robust and controllable modeling method to reconstruct the internal pore structure is fundamental for the analysis and prediction of the mechanical behavior of aluminum foam (de Giorgi et al., 2010; Xi et al., 2017).

The mechanical properties of aluminum foam, such as its strength, energy absorption capacity, and deformation behavior, are governed primarily by its internal porous architecture rather than by the base aluminum alloy alone (He et al., 2020; Zhuang et al., 2023, 2024). Key structural parameters include porosity, pore size distribution, and cell wall thickness. Porosity is widely recognized as the dominant factor influencing compressive strength and stiffness, which generally exhibit an inverse relationship with increasing porosity (Wang et al., 2020; Gölbaşı et al., 2024). However, pore size and spatial distribution are also critical. Studies indicate that foam with more uniform and finer pores tends to demonstrate more stable deformation and

✉ Lifeng FAN, fanlifeng@bjut.edu.cn
Lifeng FAN, https://orcid.org/0000-0002-7744-692X

Received Jan. 23, 2026; Revision accepted May 27, 2026;
Crosschecked June 23, 2026

© Zhejiang University Press 2026

higher energy absorption efficiency, as irregular pore arrangements can induce localized stress concentrations and trigger premature collapse under compression (Mu et al., 2010; Wang et al., 2019; Cui et al., 2025).

Pore morphology further dictates deformation mechanisms. Closed-cell foams typically display a well-defined compression plateau due to sequential cell-wall buckling and yielding, making them particularly suitable for energy-absorbing applications (Dannemann and Lankford, 2000; Teimouri and Yazdani, 2024). In contrast, open-cell foams deform mainly through cell-wall bending, lacking a distinct plateau, which leads to lower stiffness and collapse stress (Quadrini et al., 2010; Wan et al., 2021). The cell walls themselves play an equally vital role: thicker and more robust walls enhance plateau stress and energy absorption (Cheng et al., 2018; Thorat et al., 2025), whereas defects such as microcracks or thickness variations can act as failure initiators, significantly degrading mechanical performance (Guo and Wong, 2020, 2021; Hangai et al., 2020). Beyond these individual effects, synergistic interactions among parameters are significant. For example, heterogeneous structures containing adjacent regions of large and small pores can generate substantial stress gradients during loading, promoting localized deformation and reducing energy absorption efficiency (An et al., 2017; Du et al., 2025). Advanced experimental techniques such as in situ compression coupled with computed tomography (CT) have visually confirmed that collapse often initiates in high-porosity zones or areas with thin cell walls and then propagates through the structure (Hangai et al., 2025). In summary, extensive research affirms that the mechanical performance of aluminum foam is profoundly influenced by its internal structural characteristics, including pore size, wall thickness, and spatial distribution.

Given the decisive role of microstructure, numerical simulation has become indispensable for analyzing the mechanical behavior of aluminum foam. Consequently, developing modeling techniques capable of accurately reconstructing its complex internal architecture is of paramount importance. Various numerical approaches have been employed. Early studies used representative volume elements (RVEs) to replicate and stack idealized pore geometries, offering an efficient method for homogenization and macroscopic property prediction (Alsayednoor et al., 2013). While RVE models can achieve good agreement with experimental stress–strain curves under compression (Sonti et al., 2024), their inherent assumption of material homogeneity limits their ability to capture the actual heterogeneity and randomness, especially in high-porosity foams (Hamidi Ghaleh Jigh et al., 2017; Mancini et al., 2022). Fractal-based models provide an alternative, allowing control over fractal dimension and relative density, and have been applied to scenarios such as hypersonic impact. However, they often oversimplify 3D pore geometry and connectivity, requiring careful calibration (Zhang et al., 2011). The material point method (MPM) is advantageous for simulating large deformations under dynamic loading but lacks the resolution to capture detailed pore-level features (Liu et al., 2014). CT-reconstructed models, derived directly from scan data, offer high geometric fidelity and have been used to simulate compression behavior. Their drawbacks, however, include high computational cost and dependence on specific physical samples, which restricts parametric flexibility and general applicability (Ramírez et al., 2014). Random models, which distribute spherical, elliptical, or polyhedral pores throughout a volume, can mimic structural nonuniformity (Zhu et al., 2020). However, the need for pore interference checks during generation renders them computationally inefficient for creating high-porosity models (Nosko et al., 2010; Dong et al., 2025). While existing numerical methods have significantly advanced the field, a common and persistent challenge remains: precise and independent control over key geometric parameters, specifically pore size, cell wall thickness, and their distribution. This limitation is especially acute for the construction of high-porosity foam models, where conventional approaches often involve a compromise between geometric accuracy, computational efficiency, and parametric flexibility. For instance, most conventional Voronoi-based methods are constrained to porosity levels below 80% due to difficulties in maintaining cell wall connectivity at higher porosities. Similarly, although CT-based models offer high geometric accuracy, they are inherently dependent on specific physical specimens and lack the parametric flexibility required for structural variations. In addition, existing parametric models typically couple pore size and cell wall thickness, making it difficult to isolate their respective effects on mechanical behavior.

To improve modeling methods for aluminum foam, this paper proposed a modified Voronoi-based

numerical method for generating ultrahigh porosity aluminum foam models with independent control over pore size and cell wall thickness. The core of this method comprises two aspects. On the one hand, the method enables the construction of aluminum foam models with a porosity exceeding 90% while maintaining continuous and intact cell walls. On the other hand, the method introduces two independently controllable parameters, allowing for the independent control of key structural features of the model. The reliability of models constructed using the proposed method in geometric accuracy and predicting dynamic mechanical properties was validated through comprehensive comparisons with experimental samples.

2 Methodology

2.1 Parametric Voronoi-based modeling approach

The typical internal structure of closed-cell aluminum foam is primarily composed of pores and cell walls, as shown in Fig. 1. This material is characterized by a cellular solid structure consisting of pores isolated within a continuous metallic matrix. This unique structure endows the material with mechanical properties such as low density, high specific stiffness, and good energy absorption efficiency. The macroscopic mechanical properties of aluminum foam are predominantly determined by structural parameters, including pore size, cell wall thickness, and porosity. In real aluminum foam, the pores exhibit randomness in both morphology and spatial distribution, a feature crucial for constructing accurate numerical models. Therefore, it is important to precisely and efficiently control pore size and cell wall thickness in high-porosity aluminum foam models while also ensuring that the pore morphology and distribution exhibit realistic randomness.

A method for constructing aluminum foam models is proposed based on a modified approach to generating and controlling Voronoi structures. Fig. 2 illustrates the algorithmic flowchart of this method, which is used to generate a high-porosity, closed-cell aluminum foam model with controllable pore size and cell wall thickness. The modeling process mainly consists of three stages: generating a random point matrix, constructing a Voronoi polyhedral structure, and controlling the cell wall thickness. First, the process begins by generating a random point matrix. The spatial distribution of the

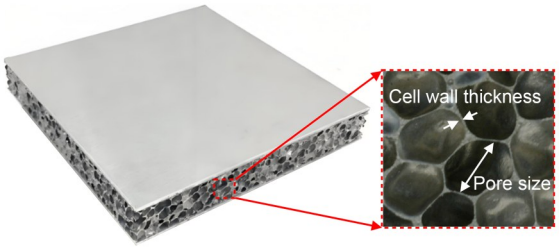


Fig. 1 Microstructure of aluminum foam

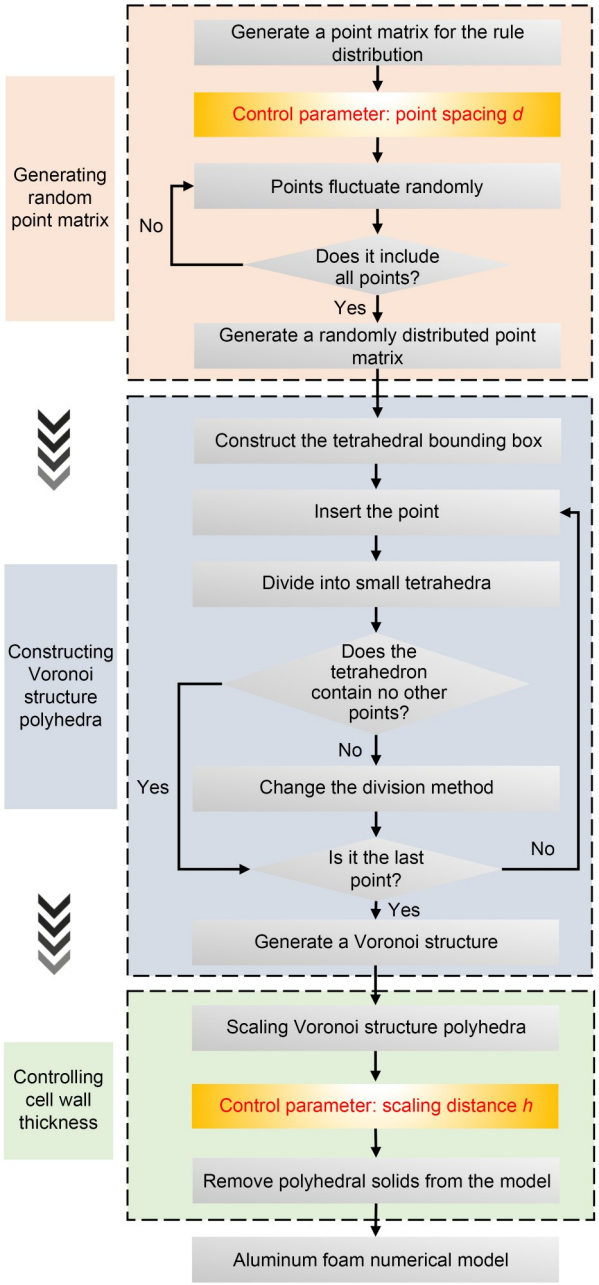


Fig. 2 Flowchart for constructing the aluminum foam numerical model

points is determined by a control parameter, the point spacing *d*, which directly dictates the average pore size of the aluminum foam model. Each point within this matrix is allowed to fluctuate randomly around its theoretical position, thereby introducing the characteristics of randomness and irregularity. Subsequently, a tetrahedral bounding box encompassing all points is constructed. The spatial domain is then systematically subdivided into small tetrahedral elements using Delaunay triangulation, ensuring that each tetrahedron contains only one point in its interior. This spatial partition forms the basis for constructing the Voronoi structure, with each resulting polyhedral element corresponding to a pore in the aluminum foam. Finally, to precisely control the cell wall thickness between adjacent pores, a critical scaling operation is applied to the generated Voronoi polyhedral structure. This operation is governed by a second control parameter, the scaling distance *h*, which shifts the walls of the polyhedral cells inward. The final numerical model of the aluminum foam is obtained via a Boolean operation between the scaled Voronoi structure and the initial base volume. This method can generate high-porosity aluminum foam models where the pore size and cell wall thickness can be independently and accurately controlled. The modeling relies on only two main parameters, the point spacing *d* and the scaling distance *h*, which ensures high efficiency.

To illustrate the generation of the aluminum foam model more intuitively, the three modeling stages are summarized as geometric transformations among four representative models. Fig. 3 illustrates the geometric

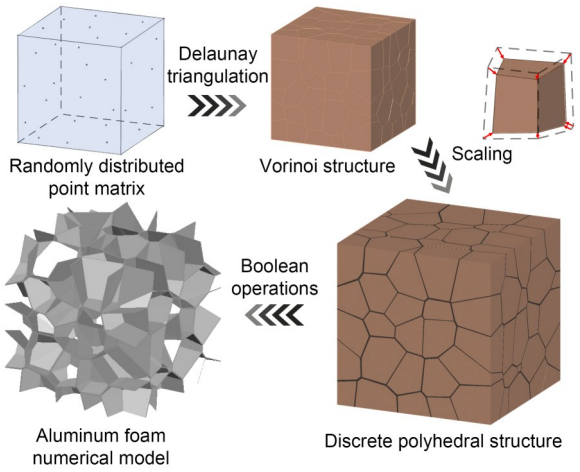


Fig. 3 Procedure for generating the aluminum foam numerical model

evolution during model generation, visually demonstrating the transformation relationships among these four models. The initial model contains only a randomly distributed point matrix. Each point in this matrix corresponds to a pore, and its spatial distribution determines the pore morphology. Subsequently, the point matrix is transformed into a Voronoi structure through Delaunay triangulation, forming the basis of the pore structure in the aluminum foam model. After this transformation, the entire initial model space is subdivided into a series of polyhedral elements, and the shape and distribution of each pore are clearly defined. Next, the geometry of each polyhedral element is modified through a scaling operation. This reduces the volumes of the polyhedral elements, generating interstitial structures with a defined geometric thickness between them, thereby forming the cell walls. Finally, Boolean operations are used to retain only these cell walls, forming the complex internal pore structure of the final aluminum foam numerical model. Boolean operations are performed on predefined geometric shapes and a scaled discrete polyhedral structure. A discrete polyhedral structure is typically set to be larger than the final numerical model to ensure that pores near the boundaries are not truncated. The resulting final aluminum foam model has the desired external shape. The generation of aluminum foam models thus primarily involves four key geometric models, which are sequentially transformed through Delaunay triangulation, scaling, and Boolean operations.

The randomly distributed point matrix is the first representative model. Fig. 4 illustrates the generation and geometric control of this matrix during the modeling process. This stage begins with a point matrix where the points are uniformly and regularly distributed. The spacing between adjacent points, denoted as *d*, controls the pore size in the final aluminum foam model. Theoretically, this can generate an idealized aluminum foam structure with uniform pore size and consistent porosity. To capture the randomness inherent in real

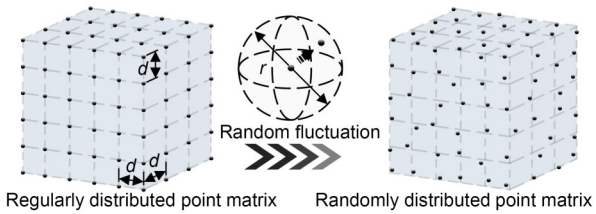


Fig. 4 Generation of the point matrix

aluminum foam, controlled random fluctuations are applied to the position of each point. The final position of each point is determined by randomly displacing it within a spherical neighborhood of radius r, thereby generating a random point matrix with specific distribution characteristics. Notably, the point spacing d determines both the size and the number of pores. A smaller point spacing d results in a higher number of points in the matrix, leading to smaller and more numerous pores. The fluctuation radius r determines the degree of irregularity in the aluminum foam. As r increases, the irregularity of the model gradually increases. The point spacing d and fluctuation radius r are treated as independent input parameters. To avoid distortion of the Voronoi cells and unrealistic pore geometries, the fluctuation radius r should generally be set to a value smaller than the point spacing d. The irregularity of the aluminum foam model can be calculated as

$$k=1-\frac{\delta_{\min}}{\delta_0}, \tag{1}$$

where k represents the irregularity of the model, $\delta_{\min}$ represents the minimum distance between adjacent points in the model, and δ_0 represents the distance between any adjacent points in a regular tetrakaidecahedral model. Both the pore size and the irregularity of the aluminum foam model are controlled through this process.

The Voronoi structure is the second representative model. Fig. 5 illustrates its construction during the modeling of aluminum foam. This process begins with the randomly distributed point matrix established in the previous stage. This matrix is transformed into a Voronoi structure that defines the porous architecture of the aluminum foam model. The topological transformation is carried out incrementally through discrete computation. First, a Delaunay triangulation is constructed based on the point matrix. Subsequently, a Voronoi structure is formed according to the principle of geometric duality. This division partitions the model space into many convex polyhedra that fill the entire space without overlap. Each polyhedron contains only one generating point, and any location within a given polyhedron is closer to its contained point than to any other point in the matrix. Each polyhedral element in the Voronoi structure is generated through this rigorous mathematical procedure, with its specific shape and size determined by the local spatial arrangement of adjacent points. This structure ultimately manifests as an interconnected network of cells that captures the stochastic morphological characteristics of real aluminum foam.

The discrete polyhedral structure is the third representative model. Fig. 6 illustrates the scaling applied to the Voronoi structure, which is a critical process for achieving precise control over the cell wall thickness. The process begins with a complete Voronoi structure composed of many compact polyhedral elements. The scaling transformation is carried out by treating the interior point of each polyhedral element as the scaling center and moving all vertices of the polyhedron inward toward this point by a fixed distance h. Notably, each polyhedron is scaled independently, thereby transforming the initially compact Voronoi structure into a discrete polyhedral model. The volume of each polyhedral element is reduced, and a continuous cell wall structure with variable thickness is formed in the interstitial regions between adjacent scaled elements. Scaling clearly delineates the pores and cell walls in the model: the scaled polyhedral elements become the pores, while the newly formed interstitial regions between adjacent contracted elements constitute the metallic cell walls. The inward scaling distance h directly determines the final cell wall thickness of the aluminum foam model. A larger scaling distance leads to thicker

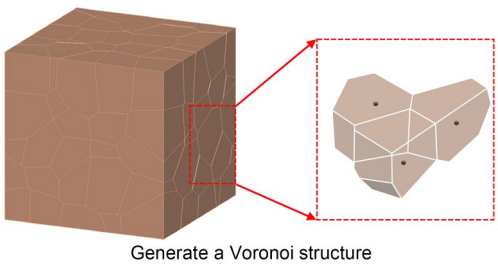


Fig. 5 Construction of the Voronoi structure

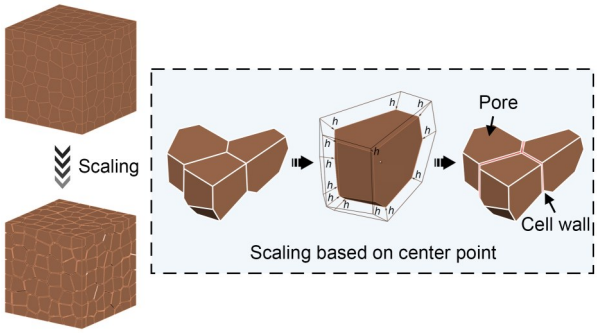


Fig. 6 Formation of the cell wall structure

cell walls. Although the scaling distance h is a constant, the resulting cell wall thickness is not uniform across the entire model. This is because the final cell wall thickness is determined not only by h but also by the local geometric configuration of the adjacent polyhedra. To ensure that the scaled polyhedron remains a valid, non-self-intersecting geometry, the scaling distance h must be smaller than the inradius (the distance from the generating point to the nearest face) of the corresponding Voronoi polyhedron. Therefore, the advantage of this scaling operation is that it maintains the random pore distribution while allowing independent control of the cell wall thickness, resulting in cell walls that themselves exhibit randomness in thickness. Finally, the aluminum foam model is generated through Boolean operation and exhibits the microstructural characteristics of closed-cell aluminum foam.

2.2 Implementation in custom modeling software

Fig. 7 illustrates the interface of the 3D aluminum foam modeling software, which integrates the proposed parametric construction method. The interface is organized into a standard operation area, a parameter control panel, and a display area. The standard operation area features a conventional menu bar containing basic commands such as open, save, exit, and view adjustment.

The parameter control panel serves as the core component of the interface, providing control over the modeling process. This panel encompasses three categories of parameters. The first category includes basic model specification parameters that define the overall dimensions of the model. The second category consists of point matrix size parameters, which control the spatial distribution of points through settings for length, width, height, and fluctuation distance. The final category comprises the critical pore control parameters, namely, the point spacing and the scaling distance, which directly determine the final pore size and cell wall thickness.

The software dynamically calculates and displays the resulting porosity of the aluminum foam model, which reaches 62.1% for the parameter combination shown. Additional features include a real-time progress indicator for model loading and a management system offering options for model display and color customization. This integrated modeling software effectively streamlines the aluminum foam model generation workflow by transforming complex geometric modeling procedures into intuitive parameter settings. It enables the efficient generation of customized aluminum foam models with specific morphological characteristics.

3 Parametric analysis and model generation

3.1 Influence of control parameters on model morphology

Fig. 8 shows the geometric morphologies of a series of aluminum foam models generated by varying

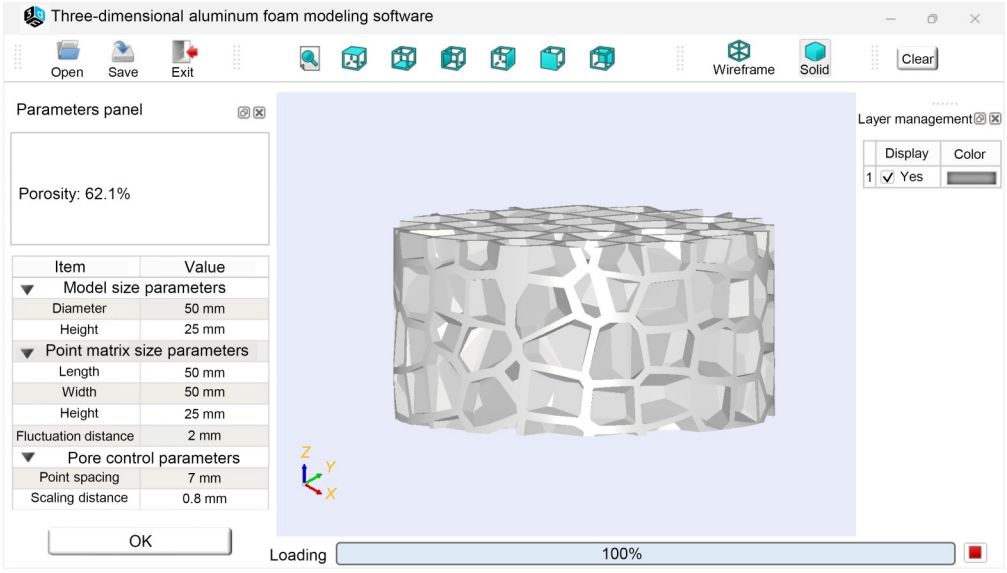


Fig. 7 Interface of the 3D aluminum foam modeling software

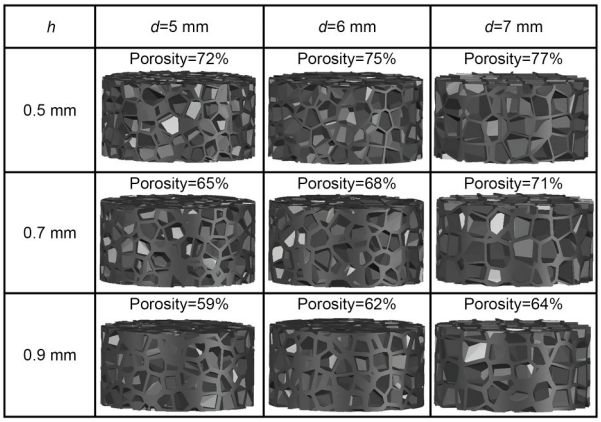


Fig. 8 Aluminum foam numerical models with different control parameters

the two primary control parameters. These two parameters, the point spacing d and the scaling distance h, independently control the internal geometric structure of the aluminum foam model. The point spacing d determines the pore size. As d increases, the overall average pore size increases, while the number of pores decreases. Similarly, the scaling distance h determines the cell wall thickness. A larger value of h results in thicker cell walls, thereby increasing the relative density of the model. For instance, for the model with d=5 mm and h=0.5 mm, the porosity is 72%. For the model with d=7 mm and h=0.9 mm, the porosity is 64%. The ability to generate aluminum foam models with distinct geometric morphologies under different parameter combinations confirms the broad applicability of the proposed method.

Fig. 9 illustrates the influence of the point spacing d and the scaling distance h on the porosity of the generated aluminum foam models. It can be observed that porosity exhibits a significant positive correlation with d. An increase in point spacing leads to larger average pore sizes, which consequently results in higher model porosity. Conversely, porosity shows a significant negative correlation with h. Cell wall thickness increases with scaling distance, which raises the volume fraction of the solid aluminum matrix and thus reduces the total porosity of the model. Furthermore, the results indicate that the effect of the scaling distance h on porosity is more pronounced when the point spacing d is smaller. The synergistic interaction between these two independently controllable parameters enables precise and predictable regulation of the final model porosity. This explicit relationship between the parameters and the porosity forms the foundation of the proposed method, allowing for the generation of aluminum foam models with prescribed porosity to meet the requirements of subsequent mechanical analysis through numerical simulations.

3.2 Generation of high-porosity foam models

Fig. 10 presents a series of aluminum foam models generated with varying pore sizes, illustrating the flexibility of the proposed method in constructing high-porosity models. The generated models cover a porosity range from 70% to 95%, achieved by setting the point spacing d to 6, 7, and 8 mm. For a given target porosity level, models with different pore sizes can be constructed. At a constant porosity, an increase in point spacing from 6 to 8 mm leads to a significant enlargement of the pore size and a corresponding reduction

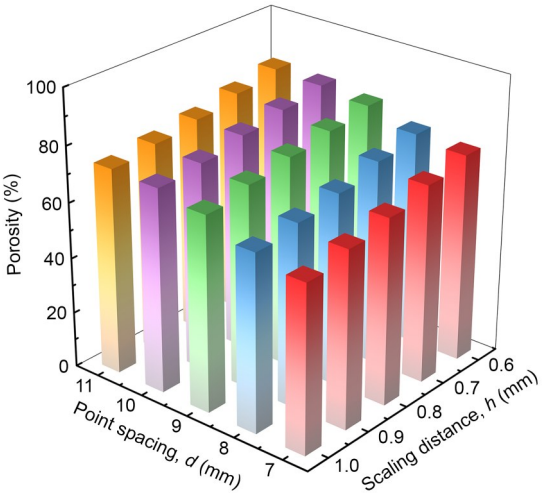


Fig. 9 Effect of control parameters on model porosity. Red: d=7 mm; blue: d=8 mm; green: d=9 mm; purple: d=10 mm; yellow: d=11 mm

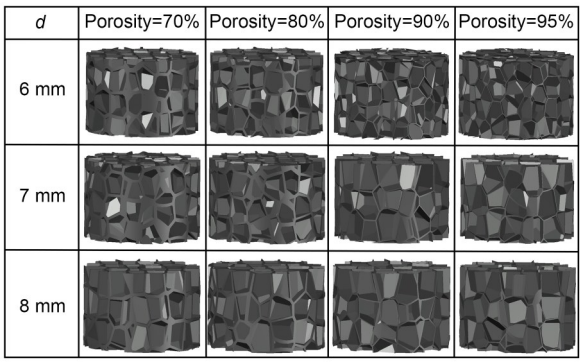


Fig. 10 High-porosity aluminum foam models with different pore sizes

in the number of pores. Conversely, for a constant pore size, an increase in porosity from 70% to 90% results in a notable decrease in cell wall thickness within the model. Despite variations in porosity and pore size, all models exhibit a similar morphological structure in their pore networks. It is noteworthy that the models maintain structural integrity even at a high porosity of 95%. Although the metallic matrix occupies a low volume fraction at this porosity, the resulting cell wall structure remains continuous and interconnected. These results demonstrate that the proposed method is capable of generating aluminum foam models across a wide spectrum of porosity and pore size combinations.

4 Model validation

4.1 Geometric accuracy

To validate the reliability of the proposed method in reconstructing the internal structure of aluminum foam, a numerical model was generated based on the geometric parameters of a real experimental sample. Fig. 11 presents a comparative view of the actual aluminum foam sample and the corresponding numerical model generated by the proposed method. Both share identical overall dimensions, with a diameter (Φ) of 50.0 mm and a height (H) of 25.0 mm. The experimental sample displays a characteristic porous structure, featuring irregular pore shapes, random spatial distribution, and nonuniform wall thicknesses. The

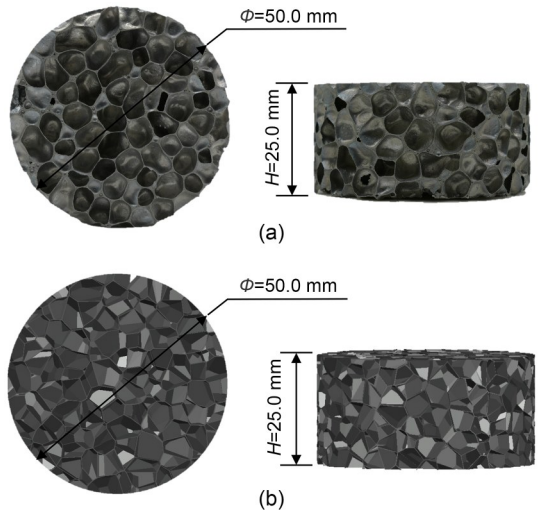


Fig. 11 Aluminum foam experimental sample and numerical model with identical dimensions: (a) aluminum foam experimental sample; (b) aluminum foam numerical model

numerical model successfully reproduces these morphological characteristics, exhibiting a comparable degree of randomness.

Fig. 12 shows the selected cross-sectional planes from both the experimental sample and the numerical model for quantitative comparison. To ensure a comprehensive analysis of the geometric morphology, two orthogonal cross-sections, labeled A–A and B–B, were extracted from each. The A–A cross-section provides a representative planar view through the central region of the cylindrical specimen, capturing the internal pore distribution and cell wall features. The B–B cross-section offers a complementary view perpendicular to A–A, revealing structural details in the third dimension. The use of these two sections ensures that the comparative analysis encompasses internal features from different spatial orientations, allowing for a more thorough evaluation of the model's geometric fidelity.

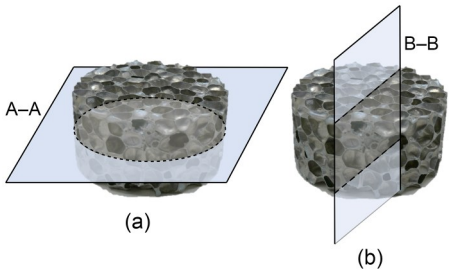


Fig. 12 Cross-sectional planes selected from the sample and numerical model: (a) A–A cross-section; (b) B–B cross-section

A quantitative comparison of pore size distribution and porosity was conducted by analyzing binarized images of the cross-sections. Fig. 13 presents a comparison of the pore size distributions in the A–A and B–B cross-sections between the experimental sample and the numerical model. As shown in Fig. 13a, pore sizes in the A–A section for both the sample and the model range from 1 to 8 mm. Their pore size distributions follow nearly identical trends: the proportion of pores initially increases and then decreases with increasing pore size. The pore sizes are primarily concentrated within the 3 to 5 mm range for both, with the highest proportion, approximately 30.08% for the sample and 30.15% for the model, found in the 4 to 5 mm range. The lowest proportion, approximately 0.74% for the sample and 0.70% for the model, is observed in the 7 to 8 mm range. Notably, the relative error in the pore size distribution between the sample and the

model remains below 10% across all size ranges. As shown in Fig. 13b, the pore size distribution trends observed in the B–B section are essentially consistent with those in the A–A section.

Furthermore, the 3D bulk porosity and the areal porosity of the cross-sections for both the sample and the model were measured, as summarized in Table 1.

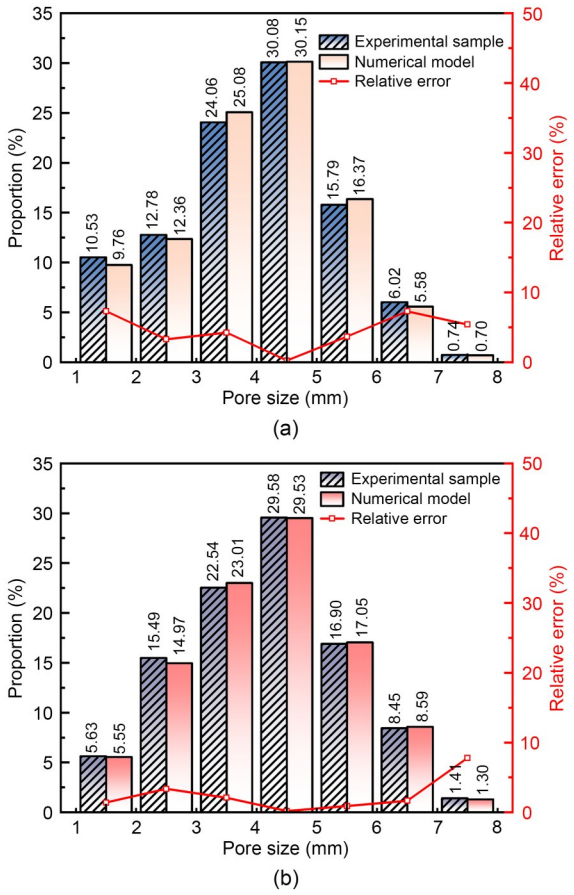


Fig. 13 Pore size distribution in cross-sections of the sample and model: (a) A–A cross-section; (b) B–B cross-section

Table 1 Porosity of the aluminum foam sample and the numerical model

Type	Porosity-3D	Porosity-2D (A–A)	Porosity-2D (B–B)
Experimental sample	76.3%	75.5%	76.8%
Numerical model	75.9%	74.5%	76.1%

The bulk porosity of the experimental sample is 76.3%, compared to 75.9% for the numerical model, yielding a relative error of 0.5%. The areal porosity values for the A–A section are 75.5% (sample) and 74.5% (model), and those for the B–B section are 76.8% (sample) and 76.1% (model). The maximum relative error for the areal porosity is 1.3%. These results indicate a strong agreement in geometric morphology between the aluminum foam sample and the numerical model across different spatial dimensions, demonstrating the geometric reliability of the models generated by the proposed method.

4.2 Dynamic mechanical performance

To validate the similarity in the dynamic mechanical properties between the aluminum foam sample and the numerical model, split Hopkinson pressure bar (SHPB) experiments and corresponding numerical simulations were performed. The geometric dimensions of the sample and model are shown in Fig. 11. In the SHPB experiment, the bullet collides with the incident bar, generating an incident stress wave that propagates along the incident bar toward the specimen. To ensure consistency between the numerical simulation and the experiment, the initial impact velocity of the bullet is set to 5 m/s in both the experiment and the numerical simulation. The matrix material of the aluminum foam is industrial pure aluminum. The porosity of the aluminum foam experimental specimen is 76%, while that of the corresponding numerical model is 75%. The mechanical behavior of the numerical model was simulated using the Johnson-Cook constitutive model and the Grüneisen equation of state, with the relevant material parameters provided in Tables 2 and 3.

Fig. 14 presents the comparative results between the SHPB experiment and the numerical simulation. Fig. 14a shows the stress histories recorded by the incident bar. In the experiment, the stress of the incident wave first decreases and then increases over time, while the reflected wave exhibits the opposite trend. The waveforms obtained from the numerical simulation show high consistency with the experimental

Table 2 Parameters of the Johnson-Cook constitutive model

Shear modulus (GPa)	Initial yield strength (MPa)	Hardening modulus (MPa)	Strain rate hardening coefficient	Strain hardening exponent	Thermal softening coefficient	Melting temperature (K)
27	35	25	0.015	0.34	1.426	933

Table 3 Parameters of the Grüneisen equation of state

Sound speed (m/s)	First Hugoniot coefficient	Linear energy coefficient	Nonlinear energy coefficient
5328	1.338	2	0

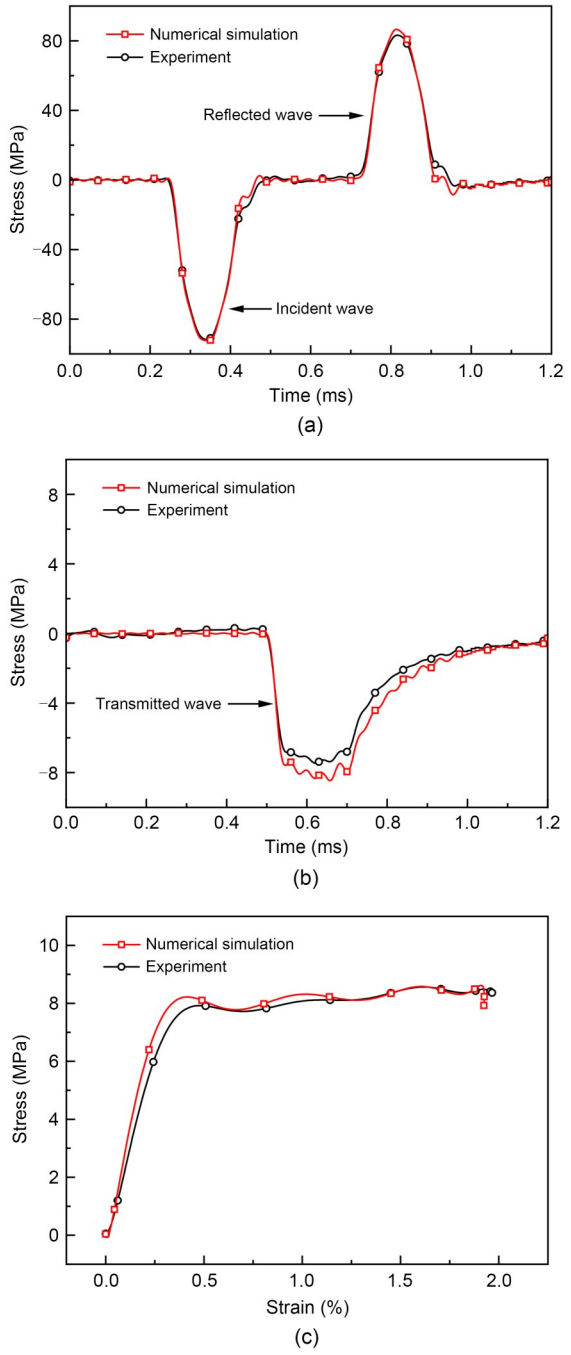


Fig. 14 Comparison of the dynamic stress–strain relationships between the sample and the model: (a) waveforms of the incident bar; (b) waveforms of the transmission bar; (c) stress–strain relationships of the sample and the numerical model

waveforms. The amplitude of the incident wave is −91.7 MPa in the experiment and −92.4 MPa in the simulation, resulting in a relative error of 0.8%. The amplitudes of the reflected wave are 83.2 MPa (experiment) and 86.6 MPa (simulation), with a relative error of 4.1%. Since the incident waves can be controlled, an extremely low relative error between the numerical simulation and the experimental results is to be expected. Meanwhile, the high similarity in the amplitude of the reflected waves indicates that the numerical model accurately reproduces the wave reflection behavior dominated by the porous structure.

Fig. 14b shows the stress histories recorded by the transmission bar. The stress of the transmitted wave in the experiment also shows an initial decrease followed by an increase over time. The variation trend of the transmitted wave in the simulation is generally consistent with the experiment. The amplitude is −7.5 MPa in the experiment and −8.5 MPa in the simulation, yielding a relative error of 13.3%. In addition, although the relative error in the transmitted wave amplitude is slightly higher, it remains within an acceptable range. The overall waveform consistency validates that the proposed modeling method captures the essential dynamic stress wave propagation characteristics of aluminum foam.

Fig. 14c shows the dynamic stress–strain curves for both the experimental sample and the numerical model. The dynamic stress–strain relationship exhibits three characteristic stages typical of cellular materials under impact loading: a linear elastic region at small strains and a relatively flat plateau region, followed by a densification region. In the experiment, the stress increases rapidly initially and then reaches a plateau region, with a yield stress of 8.5 MPa. The stress–strain relationship from the numerical simulation under dynamic impact shows high agreement with the experimental results. The yield stress of the numerical model is 8.6 MPa, corresponding to a relative error of only 1.2%. The plateau region in the simulated curve exhibits slightly smoother stress fluctuations compared to the experimental curve. This is expected because the numerical model is more idealized, whereas the real sample contains microstructural defects that cause more erratic local collapse. The various stages of the two curves are essentially consistent. These results validate the high reliability of the proposed method in predicting the complete dynamic compression response

of aluminum foam. Regarding the potential uncertainties associated with high-porosity structures in dynamic analysis, the proposed model accounts for geometric randomness through the generation of a random point matrix. Furthermore, in dynamic analysis, slight variations in local pore shapes and cell walls within high-porosity structures can lead to slight differences in the processes of cell wall buckling and local collapse. However, during the compression process, the aluminum foam numerical model and the experimental specimens exhibited consistency at all stages. This indicates that although local collapse exhibits randomness, the overall dynamic mechanical response can be well characterized.

Having validated the reliability of the numerical model for stress–strain analysis, it is necessary to further examine the influence of internal structural parameters on dynamic mechanical properties. This step is crucial for comprehensively validating the reliability of the method in analyzing the dynamic mechanical behavior of aluminum foam. Therefore, SHPB numerical simulations were conducted on aluminum foam models with different pore sizes and cell wall thicknesses. The pore size and cell wall thickness are controlled by the point spacing d and the scaling distance h, respectively.

Fig. 15a illustrates the influence of pore size on the dynamic compressive strength of models with five different cell wall thicknesses. The dynamic compressive strength decreases approximately linearly with increasing pore size. For instance, for models with a scaling distance of 1.0 mm, as the point spacing increases from 7.0 to 11.0 mm, the dynamic compressive strength decreases from 11.0 to 7.6 MPa, a reduction of 30.9%. When the cell wall thickness is constant, larger pore sizes indicate a higher porosity in the model and a smaller proportion of the aluminum matrix. This implies that the ability of aluminum foam to redistribute stress around the failure zone is reduced, making it more prone to collapse when subjected to external loads. Conversely, the dynamic compressive strength increases with increasing cell wall thickness. For models with a point spacing of 7.0 mm, increasing the scaling distance from 0.6 to 1.0 mm raises the dynamic compressive strength from 6.4 to 11.0 MPa, an increase of 71.9%. This pronounced effect highlights that cell wall thickness is a more sensitive parameter than pore size for tuning strength. Notably, the independent control of

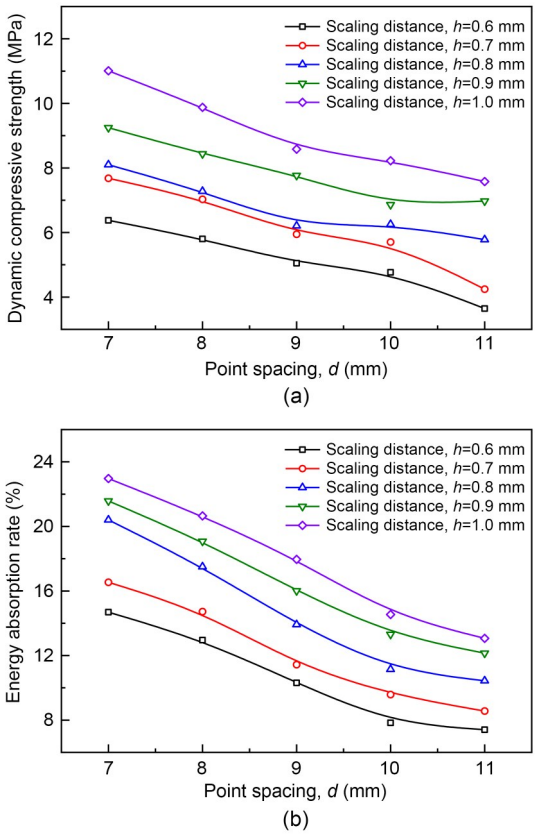


Fig. 15 Effect of pore size and wall thickness on dynamic mechanical properties: (a) dynamic compressive strength; (b) energy absorption rate

pore size and cell wall thickness provided by the proposed method allows these two effects to be quantitatively separated. These observed trends are consistent with existing experimental findings, thereby validating the reliability of the proposed method for analyzing dynamic compressive strength (Duarte et al., 2014; Aldoshan and Khanna, 2017).

The dynamic mechanical properties of aluminum foam also include its energy absorption capacity. To further validate the reliability of the method, the energy absorption rates of models with different pore sizes and cell wall thicknesses were calculated. According to the principle of energy conservation, the energy absorbed by the aluminum foam W_S can be expressed as

$$W_S = W_I - W_R - W_T, \tag{2}$$

where W_I, W_R, and W_T represent the energies of the incident, reflected, and transmitted waves, respectively. According to stress wave propagation theory, these energies are calculated as

$$\begin{cases} W_{\mathrm{I}} = EcA\int_0^t \varepsilon_{\mathrm{I}}^2 \mathrm{d}t, \\ W_{\mathrm{R}} = EcA\int_0^t \varepsilon_{\mathrm{R}}^2 \mathrm{d}t, \\ W_{\mathrm{T}} = EcA\int_0^t \varepsilon_{\mathrm{T}}^2 \mathrm{d}t, \end{cases} \tag{3}$$

where ε_{I}, ε_{R}, and ε_{T} are the strains in the bar caused by the incident, reflected, and transmitted waves, respectively. E is Young's modulus of the bar, c is the wave propagation speed in the bar, t is the time, and A is the cross-sectional area of the bar. Consequently, the energy absorption rate η of the aluminum foam is

$$\eta = \frac{W_{\mathrm{I}} - W_{\mathrm{R}} - W_{\mathrm{T}}}{W_{\mathrm{I}}} \times 100\%. \tag{4}$$

Fig. 15b illustrates the influence of pore size on the energy absorption rate for models with five different cell wall thicknesses. The energy absorption rate decreases approximately linearly with increasing pore size. For models with a scaling distance of 1.0 mm, as the point spacing increases from 7.0 to 11.0 mm, the energy absorption rate decreases from 23.0% to 13.1%, a reduction of 43.0%. On the other hand, the energy absorption rate increases with cell wall thickness. For models with a point spacing of 7.0 mm, increasing the scaling distance from 0.6 to 1.0 mm raises the energy absorption rate from 14.7% to 23.0%, an increase of 56.5%. This shows a similar trend to that of the dynamic compressive strength but with greater sensitivity, indicating that energy absorption is more significantly influenced by pore structure than compressive strength. This is consistent with the pattern observed in previous studies, which found that the energy absorption capacity of closed-cell aluminum foam increases as pore size decreases and relative density increases (Edwin Raj et al., 2009; Wang et al., 2023). The numerical simulation results comprehensively validate the reliability of the proposed method for investigating the dynamic mechanical properties of aluminum foam.

The dynamic mechanical analysis serves two primary validation purposes. On the one hand, the comparison between the numerical model and the experimental sample validates the predictive capability of the model. The numerical model accurately reproduces the dynamic stress–strain response of real aluminum foam. This consistency confirms that the model captures the fundamental mechanical behavior. On the other hand, the model established by the proposed method isolates the individual effects of two structural parameters. The parameter analysis verifies that the model can accurately predict the trends in dynamic mechanical properties as structural parameters vary, thereby providing a method for optimizing material performance.

5 Conclusions

This study proposed a method for constructing aluminum foam models that enables independent control of pore size and cell wall thickness. The effects of the two primary modeling control parameters on the geometric morphology and porosity of the aluminum foam models were investigated. The reliability of the proposed method was validated through a comparison of both geometric morphology and dynamic mechanical properties between an experimental aluminum foam sample and its corresponding numerical model.

1. The proposed method enables precise control over the pore size and cell wall thickness of aluminum foam models by adjusting the point spacing and scaling distance. The pore size of the model increases with larger point spacing, resulting in higher porosity. Conversely, the cell wall thickness increases with larger scaling distance, which raises the volume fraction of the aluminum matrix and correspondingly reduces the porosity.

2. The reliability of the modeling method has been validated in terms of geometric morphology. The relative error in porosity between the numerical model and the experimental sample is less than 3%, and the relative error in pore size distribution is less than 10%. These results indicate that the proposed method is capable of accurately reconstructing the internal geometric structure of aluminum foam.

3. The reliability of the method has also been validated in terms of dynamic mechanical properties. The relative error in yield stress between the numerical model and the experimental sample is 1.2%. Furthermore, the internal structural parameters of the aluminum foam model significantly influence its dynamic mechanical properties, which is consistent with the experimental findings. This demonstrates the capability of method for accurately analyzing the dynamic mechanical properties of aluminum foam.

Acknowledgments

This work is supported by the Deep Earth Probe and Mineral Resources Exploration-National Science and Technology Major Project (No. 2025ZD1011202).

Author contributions

Peng GUO: writing–original draft, validation, investigation and formal analysis. Hanyu CHEN: data curation and visualization. Lifeng FAN: conceptualization, writing–review & editing and funding acquisition.

Conflict of interest

Lifeng FAN is an Editorial Board member of this journal, and is NOT involved in the editorial review or the decision to publish this article. Peng GUO, Hanyu CHEN, and Lifeng FAN declare that they have no conflict of interest.

Declaration on the use of generative AI tools

The authors declare that no generative AI tools were used in the preparation of this manuscript.

Data availability

Data associated with this research are available and can be obtained by contacting the corresponding author.

References

Aldoshan A, Khanna S, 2017. Effect of relative density on the dynamic compressive behavior of carbon nanotube reinforced aluminum foam. *Materials Science and Engineering: A*, 689:17-24. https://doi.org/10.1016/j.msea.2017.01.100

Alsayednoor J, Harrison P, Guo Z, 2013. Large strain compressive response of 2-D periodic representative volume element for random foam microstructures. *Mechanics of Materials*, 66:7-20. https://doi.org/10.1016/j.mechmat.2013.06.006

An YK, Yang SY, Wu HY, et al., 2017. Investigating the internal structure and mechanical properties of graphene nanoflakes enhanced aluminum foam. *Materials & Design*, 134: 44-53. https://doi.org/10.1016/j.matdes.2017.08.031

An YK, Ma HY, Zhang JS, et al., 2021. Foaming stabilization and mechanical properties of high-toughness aluminum foam fabricated using non-thickening foaming technology. *Journal of Materials Processing Technology*, 296:117212. https://doi.org/10.1016/j.jmatprotec.2021.117212

Cheng Y, Li YX, Chen X, et al., 2018. Gas release behavior of Cu-TiH_2 composite powder and its application as a blowing agent to fabricate aluminum foams with low porosity and small pore size. *Metallurgical and Materials Transactions B*, 49(3):1014-1021. https://doi.org/10.1007/s11663-018-1240-9

Cui LP, Xu XP, Zhang Z, et al., 2025. Compression fatigue properties of closed-cell aluminum alloy foams fabricated by two-step foaming method. *Advanced Engineering Materials*, 27(9):2402769. https://doi.org/10.1002/adem.202402769

Dannemann KA, Lankford J, 2000. High strain rate compression of closed-cell aluminium foams. *Materials Science and Engineering: A*, 293(1-2):157-164. https://doi.org/10.1016/S0921-5093(00)01219-3

de Giorgi M, Carofalo A, Dattoma V, et al., 2010. Aluminium foams structural modelling. *Computers & Structures*, 88(1-2):25-35. https://doi.org/10.1016/j.compstruc.2009.06.005

Dong WY, Yang QZ, Du XM, et al., 2025. Low-velocity impact properties of SiC hollow sphere/aluminum matrix syntactic foam. *Journal of Materials Engineering and Performance*, 34(19):22449-22459. https://doi.org/10.1007/s11665-025-10836-z

Du DF, Nie XF, Sun CW, et al., 2025. Effect of TaC content on pore structure and compressive and energy absorption properties of Al/TaC foam composite. *International Journal of Metalcasting*, 19(6):3363-3377. https://doi.org/10.1007/s40962-024-01533-z

Duarte I, Vesenjak M, Krstulović-Opara L, 2014. Variation of quasi-static and dynamic compressive properties in a single aluminium foam block. *Materials Science and Engineering: A*, 616:171-182. https://doi.org/10.1016/j.msea.2014.08.002

Edwin Raj R, Parameswaran V, Daniel BSS, 2009. Comparison of quasi-static and dynamic compression behavior of closed-cell aluminum foam. *Materials Science and Engineering: A*, 526(1-2):11-15. https://doi.org/10.1016/j.msea.2009.07.017

Gölbaşı Z, Öztürk B, Beköz Üllen N, 2024. The structural and mechanical properties of open-cell aluminum foams: dependency on porosity, pore size, and ceramic particle addition. *Journal of Alloys and Compounds*, 1009:176921. https://doi.org/10.1016/j.jallcom.2024.176921

Guo TY, Wong LNY, 2020. Microcracking behavior of three granites under mode I loading: insights from acoustic emission. *Engineering Geology*, 278:105823. https://doi.org/10.1016/j.enggeo.2020.105823

Guo TY, Wong LNY, 2021. Cracking mechanisms of a medium-grained granite under mixed-mode I-II loading illuminated by acoustic emission. *International Journal of Rock Mechanics and Mining Sciences*, 145:104852. https://doi.org/10.1016/j.ijrmms.2021.104852

Hamidi Ghaleh Jigh B, Hosseini Toudeshky H, Farsi MA, 2017. Experimental and multi-scale analyses of open-celled aluminum foam with hole under compressive quasi-static loading. *Journal of Alloys and Compounds*, 695:133-141. https://doi.org/10.1016/j.jallcom.2016.10.129

Hangai Y, Kawato D, Ando M, et al., 2020. Nondestructive observation of pores during press forming of aluminum foam by X-ray radiography. *Materials Characterization*, 170:110631. https://doi.org/10.1016/j.matchar.2020.110631

Hangai Y, Omika K, Inoue M, et al., 2022. Effect of porosity of aluminum foam on welding between aluminum foam and polycarbonate plate during friction welding. *The International Journal of Advanced Manufacturing Technology*, 120(1):1071-1078. https://doi.org/10.1007/s00170-022-08835-8

Hangai Y, Sakaguchi Y, Okada K, et al., 2025. Press-forming

of aluminum foam and estimation of its mechanical properties from X-ray CT images using machine learning. *Materials Characterization*, 221:114781. https://doi.org/10.1016/j.matchar.2025.114781

He SY, Lv YN, Chen ST, et al., 2020. Gradient regulation and compressive properties of density-graded aluminum foam. *Materials Science and Engineering: A*, 772:138658. https://doi.org/10.1016/j.msea.2019.138658

He SY, Wang RC, Chen WH, et al., 2024. Microplasticity induced damping of aluminum foam. *Materials Science and Engineering: A*, 896:146290. https://doi.org/10.1016/j.msea.2024.146290

Huang B, Miao Q, Zuo XQ, et al., 2023. Sound absorption performance and mechanism of aluminum foams with double main pore-porous cell wall structure. *Advanced Engineering Materials*, 25(17):2300419. https://doi.org/10.1002/adem.202300419

Kumar R, Jain H, Sriram S, et al., 2020. Lightweight open cell aluminum foam for superior mechanical and electromagnetic interference shielding properties. *Materials Chemistry and Physics*, 240:122274. https://doi.org/10.1016/j.matchemphys.2019.122274

Liu Y, Gong WW, Zhang X, 2014. Numerical investigation of influences of porous density and strain-rate effect on dynamical responses of aluminum foam. *Computational Materials Science*, 91:223-230. https://doi.org/10.1016/j.commatsci.2014.05.002

Mancini E, Campana F, Pilone D, et al., 2022. Definition of a unified material model for cellular materials with high morphological and topological dispersion: application to an AA7075-T6 aluminium foam. *Materials Science and Engineering: A*, 833:142346. https://doi.org/10.1016/j.msea.2021.142346

Mu YL, Yao GC, Liang LS, et al., 2010. Deformation mechanisms of closed-cell aluminum foam in compression. *Scripta Materialia*, 63(6):629-632. https://doi.org/10.1016/j.scriptamat.2010.05.041

Nosko M, Simančík F, Florek R, 2010. Reproducibility of aluminum foam properties: effect of precursor distribution on the structural anisotropy and the collapse stress and its dispersion. *Materials Science and Engineering: A*, 527(21-22):5900-5908. https://doi.org/10.1016/j.msea.2010.05.073

Quadrini F, Guglielmotti A, Squeo EA, et al., 2010. Laser forming of open-cell aluminium foams. *Journal of Materials Processing Technology*, 210(11):1517-1522. https://doi.org/10.1016/j.jmatprotec.2010.04.010

Rajendran R, Moorthi A, Basu S, 2009. Numerical simulation of drop weight impact behaviour of closed cell aluminium foam. *Materials & Design*, 30(8):2823-2830. https://doi.org/10.1016/j.matdes.2009.01.026

Ramírez JF, Cardona M, Velez JA, et al., 2014. Numerical modeling and simulation of uniaxial compression of aluminum foams using FEM and 3D-CT images. *Procedia Materials Science*, 4:227-231. https://doi.org/10.1016/j.mspro.2014.07.609

Sonti KSM, Penumakala PK, Narala SKR, et al., 2024. Experimental and numerical analysis of the compression behavior of aluminum syntactic foams reinforced with alumina hollow particles. *Engineering Structures*, 300:117144. https://doi.org/10.1016/j.engstruct.2023.117144

Teimouri B, Yazdani M, 2024. Closed-cell aluminum foams with spherically-adjustable pores: numerical and experimental investigation of effective parameters. *Proceedings of the Institution of Mechanical Engineers, Part B: Journal of Engineering Manufacture*, 238(10):1421-1434. https://doi.org/10.1177/09544054231202419

Thorat M, Kumar G, Sahu SN, et al., 2025. Cell wall fracture in shock-loaded aluminum foams. *Journal of Materials Engineering and Performance*, 34(12):10810-10818. https://doi.org/10.1007/s11665-024-09878-6

Wan T, Liu Y, Zhou CX, et al., 2021. Fabrication, properties, and applications of open-cell aluminum foams: a review. *Journal of Materials Science & Technology*, 62:11-24. https://doi.org/10.1016/j.jmst.2020.05.039

Wang NZ, Maire E, Chen X, et al., 2019. Compressive performance and deformation mechanism of the dynamic gas injection aluminum foams. *Materials Characterization*, 147:11-20. https://doi.org/10.1016/j.matchar.2018.10.013

Wang NZ, Chen X, Maire E, et al., 2020. Study on cell deformation of low porosity aluminum foams under quasi-static compression by X-ray tomography. *Advanced Engineering Materials*, 22(10):2000264. https://doi.org/10.1002/adem.202000264

Wang Y, Chen FX, Wang X, et al., 2023. Micro-CT in the mechanical properties and energy absorption of closed-cell aluminium foam. *Materials Today Communications*, 37:106962. https://doi.org/10.1016/j.mtcomm.2023.106962

Xi HF, Tang LQ, Luo SH, et al., 2017. A numerical study of temperature effect on the penetration of aluminum foam sandwich panels under impact. *Composites Part B: Engineering*, 130:217-229. https://doi.org/10.1016/j.compositesb.2017.07.044

Xu HH, Luo HC, Zhang XG, et al., 2023. Mechanical properties of aluminum foam filled re-entrant honeycomb with uniform and gradient designs. *International Journal of Mechanical Sciences*, 244:108075. https://doi.org/10.1016/j.ijmecsci.2022.108075

Zhang XT, Jia GH, Huang H, 2011. Numerical investigation of aluminum foam shield based on fractal theory and node-separation FEM. *Chinese Journal of Aeronautics*, 24(6):734-740. https://doi.org/10.1016/S1000-9361(11)60086-1

Zhu YX, Luo GQ, Zhang RZ, et al., 2020. Numerical simulation of static mechanical properties of PMMA microcellular foams. *Composites Science and Technology*, 192:108110. https://doi.org/10.1016/j.compscitech.2020.108110

Zhuang WM, Wang EM, Zhang HL, 2023. Prediction of compressive mechanical properties of three-dimensional mesoscopic aluminium foam based on deep learning method. *Mechanics of Materials*, 182:104684. https://doi.org/10.1016/j.mechmat.2023.104684

Zhuang WM, Wang EM, Zhang HL, 2024. Prediction of the compressive mechanical properties and reverse structural design of two-dimensional mesoscopic aluminum foam based on deep learning methods. *Journal of Materials Science*, 59(25):11416-11439. https://doi.org/10.1007/s10853-024-09866-0